AGU PUBLICATIONS

JGR

Journal of Geophysical Research: Space Physics

RESEARCH ARTICLE

10.1002/2014JA020497

Key Points:
- X-ray imaging is first suggested as promising observation technique to study KHW
- A method is proposed to extract KHW-induced signal from the X-ray intensity map
- Based on MHD simulation, global features of KHW are revealed using this method

Correspondence to:
T. R. Sun,
trsun@spaceweather.ac.cn

Citation:
Sun, T. R., C. Wang, F. Wei, and S. Sembay (2015), X-ray imaging of Kelvin-Helmholtz waves at the magnetopause, *J. Geophys. Res. Space Physics*, *120*, doi:10.1002/2014JA020497.

Received 11 AUG 2014
Accepted 8 DEC 2014
Accepted article online 15 DEC 2014

X-ray imaging of Kelvin-Helmholtz waves at the magnetopause

T. R. Sun[1,2], C. Wang[1], F. Wei[3], and S. Sembay[4]

[1]State Key Laboratory of Space Weather, National Space Science Center, Chinese Academy of Sciences, Beijing, China, [2]CAS Key Laboratory of Geospace Environment, University of Science and Technology of China, Chinese Academy of Sciences, Hefei, China, [3]Laboratory of Space Environment Exploration, National Space Science Center, Chinese Academy of Sciences, Beijing, China, [4]Department of Physics and Astronomy, University of Leicester, Leicester, UK

Abstract This paper simulates the Kelvin-Helmholtz wave (KHW)-induced X-ray emissions at the low-latitude magnetopause based on a global MHD code. A method is proposed to extract the KHW information from the X-ray intensity measured by a hypothetical X-ray telescope onboard a satellite assumed with a low Earth orbit. Specifically, the X-ray intensity at high latitude is subtracted from the intensity map as a background to highlight the role of KHW. Using this method, global features of KHW such as the vortex velocity, perturbation degree, spatial distribution, and temporal evolution could be evaluated from the X-ray intensity map. The validity of this method during intervals of solar wind disturbances is also verified. According to the simulation results, X-ray imaging of KHW is suggested as a promising observation technique to essentially "see" the large-scale configuration and evolution of KHW for the first time.

1. Introduction

The solar wind charge exchange (SWCX) process occurs when a high charge state solar wind ion (e.g., O^{7+}) encounters a neutral atom or molecule (e.g., H) and picks up an electron in an excited state, as illustrated by equation (1).

$$O^{7+} + H \rightarrow O^{6+*} + H^{+} \quad (1)$$

The ion then emits a photon when it decays to a lower energy state and thus may lead to the satellite detection of soft X-rays. Indeed, charge exchange X-ray emission from comets and planets in the solar system has been reported (reviewed by *Bhardwaj et al.* [2007]), such as the Röntgen satellite (ROSAT) observations of the comet Hyakutake [*Lisse et al.*, 1996], XMM-Newton detections of the Mars [*Dennerl et al.*, 2006], and a recent report on SWCX emission from the tenuous lunar atmosphere [*Collier et al.*, 2014].

In the geospace environment, the neutral atoms required in the SWCX process can be provided by the exospheric (geocoronal) hydrogen [*Cox*, 1998]. Consequently, X-rays are emitted in the magnetosheath and cusp region where solar wind ions collide with geocoronal hydrogen. By analyzing XMM-Newton data, *Snowden et al.* [2009] not only validated the SWCX X-ray emission from the subsolar magnetosheath but also demonstrated that this X-ray emission can be apparent even during moderate solar wind flux levels. *Carter et al.* [2010] reported geocoronal SWCX emissions along the direction pointing toward the flank magnetosheath during a coronal mass ejection interval. SWCX X-ray signals from the magnetic pole direction were also observed by Suzaku [*Fujimoto et al.*, 2007; *Ezoe et al.*, 2011].

Superposed on the extragalactic, galactic, and heliospheric sources of diffuse X-rays, SWCX X-ray emissions in the geospace environment may be hard to identify at first glance. Consequently, efforts have been made to extract the geocoronal SWCX X-ray from the total X-ray counting rate observed by an X-ray telescope. Basically, three characteristics of the geocoronal SWCX emissions help the identification. First, the SWCX spectrum has the feature of line-band emissions, corresponding to respective ion species in the solar wind such as C_V, O_{VII}, Ne_X [*Carter et al.*, 2010]. Observations of SWCX emission show less correlation between the line and continuum bands according to *Carter and Sembay* [2008]. Second, the geocoronal SWCX emissions have high time variability owing to changes in the solar wind [*Cravens et al.*, 2001]. Given that most of the temporal variations of the observed X-ray can be attributed to geocoronal SWCX, the steady parts of the diffuse X-ray sources can be filtered out [*Carter et al.*, 2011]. Third, as the solar wind flux increases

©2014. American Geophysical Union. All Rights Reserved.

to high levels, the geocoronal SWCX contribution increases nonlinearly and can dominate the other sources [*Robertson and Cravens*, 2003a]. Comparison between X-ray observations under high and low solar wind flux leads to the unambiguous recognition of geocoronal SWCX emissions [*Fujimoto et al.*, 2007; *Ezoe et al.*, 2011; *Carter et al.*, 2010]. Moreover, the dark moon can also be used to block out the other sources of the soft X-ray background, and *Wargelin et al.* [2004] used this method to show firm evidence for the geocoronal SWCX in Chandra data [see also *Collier et al.*, 2014]. Properly extracted SWCX X-rays contain valuable information on solar activity and its interaction with the geospace environment [e.g., *Ezoe et al.*, 2011].

Although the SWCX emission exists all the time, as detected by ROSAT as the long-term enhancement part of diffuse soft X-ray [*Cravens et al.*, 2001], observational studies focusing on geocoronal SWCX X-rays are sporadic and limited, since the astronomical missions are designed to achieve astronomical science objectives, and thus are only suitable to observe the region with strongest geocoronal SWCX emissions at limited times of the year [*Carter and Sembay*, 2008]. Moreover, most satellites have a quite narrow field of view (FOV) and thus fail to provide large-scale imaging of the geospace environment. Although X-ray telescopes making use of the Lobster eye optics can provide a large FOV [*Peele et al.*, 2004], they have never been applied to magnetospheric observations. Therefore, the X-ray emissions from the magnetosphere are mostly studied theoretically by using numerical studies. *Robertson and Cravens* [2003b] modeled the X-ray emission from the magnetosheath and provided clear outlines of the bow shock and magnetopause in the image of the X-ray intensity. *Robertson et al.* [2006] further developed their model by using the 3-D BATSRUS MHD model, which illustrates an evident enhancement of the X-ray intensity in the cusp region.

Although simulations of SWCX emissions from the steady state magnetosheath and cusp were performed, transient phenomenon developing on the magnetopause boundary layer [*Collier et al.*, 2010] such as the Kelvin-Helmholtz wave (KHW) has been scarcely discussed. If two fluids have a sufficient velocity difference, a fundamental process named Kelvin-Helmholtz (KH) instability tends to occur at their interface. On the magnetopause, KHW has been widely reported by in situ observations, as the magnetosheath flow is faster than the relatively stagnant magnetospheric plasma [e.g., *Hasegawa et al.*, 2004; *Taylor et al.*, 2012; *Nishino et al.*, 2011]. In addition to the flow shear, other factors such as the magnetic field direction also have influences on the development of KHW. With favorable conditions, the KHW can grow to form rolled-up vortices [e.g., *Guo et al.*, 2010; *Li et al.*, 2013] and consequently transport energy, momentum, and plasma from the solar wind to the magnetosphere. Therefore, KHW is significant to the dynamics of the solar wind-magnetosphere coupling. In situ measurements are indicative of local features and kinetic processes of KHW [e.g., *Hasegawa et al.*, 2004] but fail to reveal its global configuration and large-scale dynamics. This paper simulates the X-ray imaging of the KHW on the magnetopause as viewed from a hypothetical X-ray telescope using the 3-D PPMLR-MHD code [*Hu et al.*, 2007]. Model description is given in section 2, and the global features of KHW evaluated from X-ray imaging are presented in section 3. We end this paper with discussion and conclusion in sections 4 and 5.

2. Method Description

2.1. X-ray Intensity of the Geocoronal SWCX Emission

The X-ray intensity of the geocoronal SWCX emission for a particular line of sight (I) can be estimated by the line integration of volume emission rate (P) [*Cravens*, 2000]:

$$I = \frac{1}{4\pi}\int P\mathrm{d}r = \frac{1}{4\pi}\int \alpha n_H n_{sw}\langle g\rangle \mathrm{d}r \quad (\mathrm{keV\ cm^{-2}\ s^{-1}\ sr^{-1}}), \tag{2}$$

where the efficiency factor α is defined as $\alpha = \sum_s f_s \sum_q f_{sq}\sigma_{sq}\sum_j f_{sqj}\Delta E_{sqj}$ [*Cravens*, 1997]. The sums are over heavy solar wind ion species s, the charge state q within that species, and the transition index j for s and q. f_s, f_{sq}, and f_{sqj} are the fraction of species s in the solar wind, the fraction of charge state q in species s, and the probability of emission by species s and charge state (q-1) in transition j, respectively. ΔE_{sqj} is the energy of the transition, and σ_{sq} is the charge transfer cross section between s and q with collision speed $\langle g\rangle$. Therefore, the α factor combines the contributions from various line emissions. *Cravens* [2000] gave a rough estimate of α as 6×10^{-16} to 6×10^{-15} eV cm^2. *Pepino et al.* [2004] then determined that for solar wind with the speed of 300-600 km/s, α is 9.38×10^{-16}, and for faster solar wind with the speed of 600–800 km/s, α is 3.33×10^{-16}. *Cravens et al.* [2001] used $\alpha = 1.5\times10^{-15}$ in their simulation of SWCX X-ray from energy band ~ 100 eV to 1 keV under average solar wind speed [*Robertson and Cravens*, 2003b]. This paper adopts $\alpha = 1\times10^{-15}$ eV cm^2 for the simulation under a normal solar wind speed (400 km/s). n_H and n_{sw}

©2014. American Geophysical Union. All Rights Reserved.

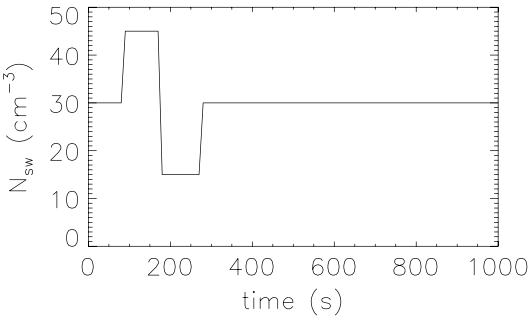

Figure 1. Time variation of the solar wind number density at the inflow boundary ($x = 30\ R_E$) of the PPMLR-MHD code used in this study.

in equation (2) are number densities of the exospheric hydrogen and solar wind proton, respectively. A reasonable approximation of n_H is $n_H = 25\ (cm^{-3})(10(R_E)/r)^3$ [*Cravens et al.*, 2001]. The $\langle g \rangle$ is the collision speed estimated by the solar wind speed u_{sw} and thermal speed u_{th}: $\langle g \rangle = \sqrt{u_{sw}^2 + u_{th}^2}$. Integration of P over the line of sight starts from the inner boundary of the magnetopause boundary layer to $r = 80\ R_E$, instead of starting from the satellite position since SWCX basically does not occur inside the magnetopause. Although there is access of solar wind particles into the magnetosphere, direct calculation can justify that the X-ray intensity inside the magnetosphere is at least an order of magnitude smaller than that outside, assuming that the effective entry rate is 10^{27} particles per second [*Li et al.*, 2008]. Geocoronal SWCX emission beyond 80 R_E is neglected as the density of geocoronal hydrogen drops dramatically there.

2.2. PPMLR MHD Model for the Magnetospheric System

The solar wind-magnetosphere system is simulated by using the 3-D PPMLR (extended Lagrangian version of the piecewise parabolic method) MHD code developed by *Hu et al.* [2007]. The low dissipation of this numerical method (PPM) favors the development of KHW even under steady solar wind parameters [*Li et al.*, 2013]. In this paper, the Earth's dipole tilt is set to be zero and the ionosphere is simplified as a spherical shell with a uniform Pedersen conductance and a zero Hall conductance. The numerical domain extends from 30 to −300 R_E along the x axis and from 0 to 150 R_E in y and z directions of the geocentric solar magnetospheric (GSM) coordinate, with the minimum grad spacing of 0.1 R_E.

The present study adopts the following solar wind conditions: solar wind speed $v_x = 400$ km/s, and $v_y = v_z = 0$; IMF $B_x = B_y = 0$ and $B_z = 2$ nT. Solar wind disturbances are introduced during the calculation by changing the plasma number density N_{sw} in the inflow boundary at 30 R_E according to Figure 1, in order to simulate the KHW-induced fluctuations of X-ray intensity superposed on the variations caused by solar wind disturbances. The purpose of introducing a disturbance of N_{sw} is to verify whether the KHW information can be successfully extracted under variations of solar wind conditions. Solar wind number density, roughly proportional to X-ray emissivity, is relatively higher than average in this simulation.

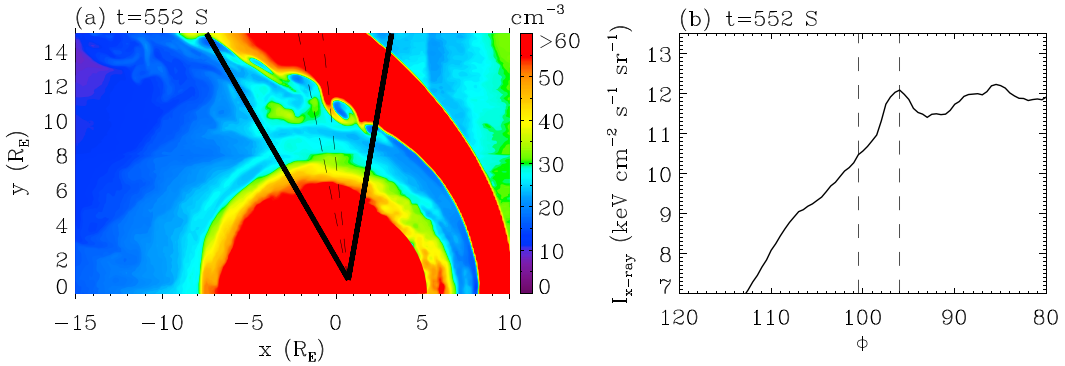

Figure 2. (a) Contours of number density showing the KHW in the equatorial plane; (b) integrated X-ray intensity in the equatorial plane. In Figure 2a, places around the inner boundary of the code at $r = 3\ R_E$ are blocked by red regions in the figure as the study on KHW emphasizes the magnetopause boundary layer. The longitudinal range of the FOV is marked by the two thick lines, i.e., from $\phi = 80$ to 120°. The two dashed lines show two typical lines of sight with an expected maximum and minimum X-ray intensity, respectively. In Figure 2b, the two vertical dashed lines correspond to dashed lines in Figure 2a, respectively.

©2014. American Geophysical Union. All Rights Reserved.

3. Numerical Results

This section presents the simulated X-ray intensity seen by a hypothetical X-ray telescope onboard a satellite assumed with a low Earth orbit (LEO). We choose a point in the LEO with a height of 600 km: (0.69, 0.85, and 0.) R_E, and direct the telescope from this point toward the dusk flank of the magnetopause. A wide FOV is adopted: 40 × 40°. The latitudinal range of the FOV covers from $\theta = 0$ to 40°, where θ is the angle between line of sight and the equatorial plane. In the longitudinal orientation, we define ϕ as the angle between the Earth-Sun direction and the projection of the line of sight on the equatorial plane. The FOV ranges from $\phi = 80$ to 120°, as shown by the two thick lines in Figure 2a. Figure 2a depicts the contours of plasma number density in the equatorial plane. KH vortices develop in the flank magnetopause as shown in the figure. Several high-density spikes intrude from the magnetosheath into the magnetosphere, indicating the KHW-induced transportation of solar wind plasma toward the magnetosphere, or the mixture of the magnetosheath and magnetospheric plasma in the magnetopause boundary layer. Since the X-ray intensity is proportional to n_{sw} based on equation (2), it is expected that the line of sight traversing the high-density spike, as shown by the right-side dashed line in Figure 2a, corresponds to larger X-ray intensity compared to other directions such as the one shown by the left dashed line. This is the basis on which we extract the KHW information analyzed below.

As expected, the X-ray intensity in the equatorial plane (Figure 2b) shows local maxima along the lines of sight traversing the KH vortices. The local maximum is superposed on an X-ray background which decreases toward the nightside. To clearly reveal the KHW features, the KHW-induced maximum should be extracted from this background. The polynomial fitting of this background might be the first method that comes into mind, while after a second thought, function fitting tends to complicate the problem when disturbances occur in the solar wind proton flux or the heavy ion abundances. An appropriate method is thus needed.

3.1. The Method to Extract KHW Information

MHD simulations [*Li et al.*, 2013] showed that KHW mainly develops at low latitudes, and its growth rate significantly decreases toward high latitudes [*Contin et al.*, 2003]. Therefore, by choosing a plane with a relatively high θ angle (θ_h) as a reference, the difference of the X-ray intensity between this plane and planes with lower latitudes reasonably approximates the KHW-induced signal dI:

$$\mathrm{d}I(\phi,\theta) = I(\phi,\theta) - I(\phi,\theta_h). \tag{3}$$

By presenting the development of a typical KH vortex from $t = 850$ s (left column) to 954 s in Figure 3 (right column), we illustrate the X-ray intensity map of KHW. Solid and dotted lines in Figures 3a1 and 3b1 are the integrated X-ray intensity in the planes with $\theta = 0°$ and 40° respectively. It is shown that the X-ray intensity in the equatorial plane has a local maximum (vertical dashed line), which disappears at the high latitude, resulting from the confinement of KHW to the low-latitude regions. Figures 3a2 and 3b2 illustrate the KH vortices on the magnetopause boundary layer by showing contours of plasma number density in the equatorial plane. By contrast, KHW features could not be identified from contours of N in the plane with $\theta = 40°$ in Figures 3a3 and 3b3. Therefore, the X-ray intensity in this plane shown by dotted lines in Figures 3a1 and 3b1 is absent of the KHW-induced local maximum and hence can be subtracted to highlight KHW signals, i.e., $\theta_h = 40°$ in equation (3). Contours of d$I(\phi,\theta)$ are plotted in Figures 3a4 and 3b4. It is revealed that the warm-colored region corresponds well with the KH vortex marked by the dashed line. Aside from the apparent tailward propagation of the KHW, one can also tell from the X-ray intensity map the decrease of maximum dI and the diffusion of KH vortex from t 850 s to 954 s. This indicates the weakening of KHW activity, i.e., the perturbation amplitude of plasma density and/or velocity caused by KHW in the low-latitude boundary layer decreases.

3.2. KHW Features Viewed From the X-ray Image

Before presenting the quantitative features of KHW, several parameters are defined at first. The angle ϕ_{meq} is the ϕ angle of the maximum dI in the equatorial plane, roughly marking the longitudinal position of the KH vortex. The parameter dI_{meq} is the maximum value of dI in the equatorial plane, implying to what degree are the sheath plasma rolled up by KHW. The latitudinal boundary of the KH vortex is approximately demonstrated by θ_b, defined as the θ angle at which d$I(\phi,\theta)$ decreases to a certain proportion (i.e., 50%) of dI_{meq}.

©2014. American Geophysical Union. All Rights Reserved.

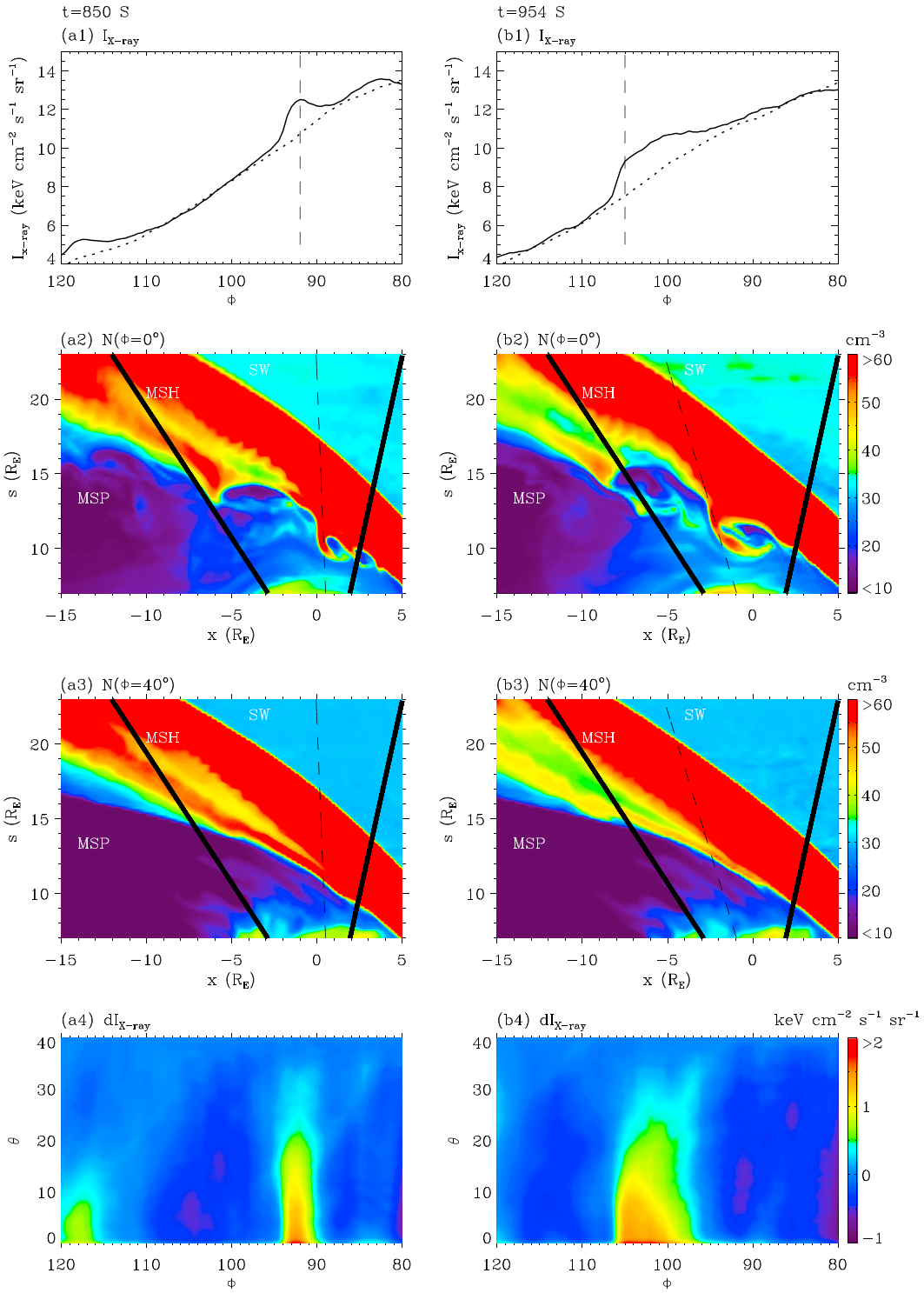

Figure 3. The development of a typical KH vortex from (a1–a4) t = 850 s to (b1–b4) 954 s. In Figures 3a1 and 3b1, the solid and dotted lines show the integrated X-ray intensity in the equatorial plane and the plane with $\theta = 40°$, respectively. Vertical dashed line indicates the KHW-induced local maximum. Figures 3a2 and 3b2 are contours of plasma number density in the equatorial plane; contours of N on the plane with $\theta = 40°$ are plotted in Figures 3a3 and 3b3. The solar wind, magnetosheath, and the magnetosphere regions are denoted by SW, MSH, MSP, respectively. Solid lines mark the edges of FOV, and the dashed line is the line of sight traversing the KH vortex. Figures 3a4 and 3b4 are the contours of $dI(\phi, \theta)$ (in keV cm^{-2} s^{-1} sr^{-1}) inside the FOV.

©2014. American Geophysical Union. All Rights Reserved.

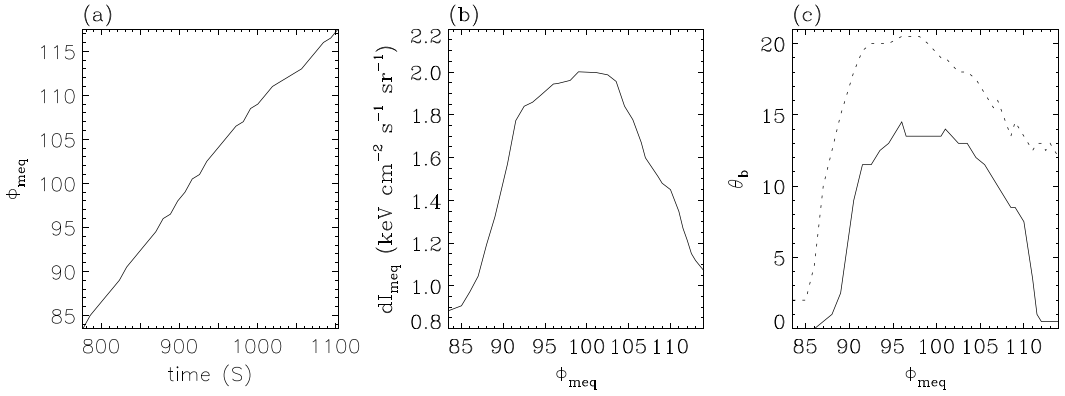

Figure 4. The relationship between (a) ϕ_{meq} and time, dI_{meq} and (b) ϕ_{meq}, as well as (c) θ_b and ϕ_{meq}. Solid and dotted lines in Figure 4c are the boundaries with $dI(\phi, \theta)$ decreasing to 50% and 30% of dI_{meq}, respectively.

Figure 4a shows the temporal evolution of ϕ_{meq} for a typical KH vortex (the one portrayed in Figure 3). It is revealed that the vortex moves tailward with a roughly constant angular velocity, i.e., $\omega = 0.10°/s \approx 0.0017$ rad/s according to the linear fit. As the geocentric distance of the magnetopause boundary layer r_{mp} increases toward the tail, the line speed of the KH vortex ($v = \omega \cdot r_{mp}$) enhances, from $v \approx 0.0017$ rad/s $\times$ 12 $R_E \approx$ 133 km/s at the flank to $v \approx 0.0017$ rad/s $\times$ 17 $R_E \approx$ 189 km/s near the tailward edge of the FOV. The relationship between dI_{meq} and ϕ_{meq} is plotted in Figure 4b. Before the vortex arrives at the terminator plane, dI_{meq} increases sharply antisunward, indicating the rapid development of KHW. The vortex reaches its highest level between $\phi_{meq} \sim$ 91 and ~104°, with the maximum value $dI_{meq} = 2.0$ keV cm^{-2} s^{-1} sr^{-1} at $\phi_{meq} = 99°$. Afterward, dI_{meq} rapidly decreases tailward. This suggests that the maximum perturbation weakens when $\phi_{meq} > 104°$ as the longitudinal scale of the rolled-up KH vortex expands (Figure 3), probably due to the stabilization effect of the magnetic field [*Cowee et al.*, 2010]. Figure 4c illustrates how θ_b varies with ϕ_{meq}. Solid and dotted lines are the vortex boundaries with the high latitude dI decreasing to 50% and 30% of dI_{meq}, respectively. The latitudinal scale of the vortex peaks around ~91 to 104°, corresponding to the place where the vortex has highest level of dI_{meq} in Figure 4b. Both Figures 4b and 4c imply that the KH vortex develops to its mature stage slightly tailward of the flank magnetopause, where it has the largest latitudinal scale and highest perturbation amplitude.

3.3. KHW Signal During Solar Wind Disturbances

For realistic situations, solar wind parameters and the heavy ion abundances are not constants. They also lead to variations of the X-ray intensity, in addition to the development of KHW. This section analyzes the performance of the above method when the solar wind disturbance front in the magnetosheath and a KH vortex are along the same line of sight and concludes that the KHW signal can be successfully extracted during this interval.

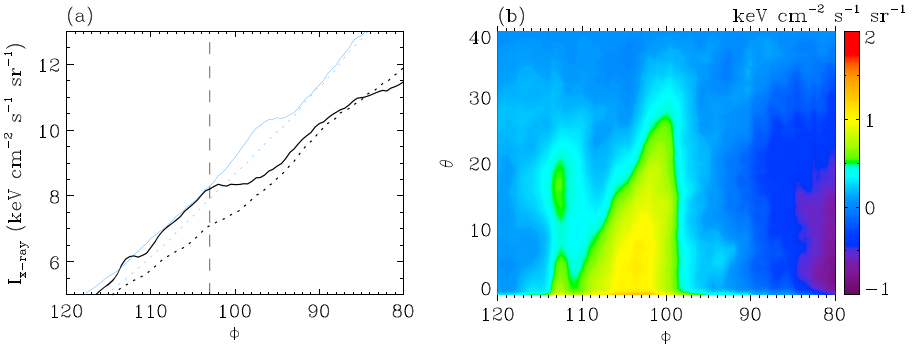

Figure 5. (a) X-ray intensity in the equatorial plane (solid lines) and the plane with $\theta = 40°$ (dotted lines). Blue/black lines are the values at $t = 402/711$ *s* before/during the arrival of the solar wind disturbance. The vertical dashed line marks the position of a KH vortex developed during solar wind perturbation. (b) Contours of $dI(\phi, \theta)$ (in keV cm^{-2} s^{-1} sr^{-1}) inside the FOV at $t = 711$ s.

©2014. American Geophysical Union. All Rights Reserved.

Figure 5a shows the X-ray intensity in the equatorial plane (solid lines) and the plane with $\theta = 40°$ (dotted lines). Blue lines are plotted at $t = 402$ s before the solar wind disturbance, while the black lines are drawn at $t = 711$ S when the decreasing edge of the solar wind number density shown in Figure 1 passes the direction with $\phi \sim 103°$, as evident from the two dotted lines in Figure 5a. From the black solid line alone, it is difficult to determine which factor is responsible for the local maximum of I_{X-ray} marked by the vertical dashed line: the arrival of the solar wind disturbance front with decreasing N_{sw} or a KH vortex developing there. However, the influence of the solar wind disturbance can be eliminated by subtracting the X-ray intensity in the plane with $\theta = 40°$ assuming the rotational symmetry of the magnetosheath about the X axis. The KHW signal (Figure 5b) is thus extracted, which is confirmed by contours of number density in the equatorial plane (not shown). Nevertheless, it should be noted that this method may fail if the normal of the disturbance front apparently deviates from the equatorial plane.

4. Discussion

4.1. More Information About KHW

In addition to the features analyzed above, more information about KHW may be obtained via X-ray imaging of the magnetopause. For instance, dawn-dusk asymmetry of KHW [*Taylor et al.*, 2012] may be observed by looking at the dawn and dusk magnetopause in turn. By changing the FOV in the latitudinal direction, it is possible to examine under what conditions can KHW develop in higher latitudes [*Hwang et al.*, 2012]. In addition, the relationship between solar wind parameters and the KHW development might also be studied. Provided that X-ray imaging of KHW is feasible, more global characteristics of KHW difficult to detect with in situ observation can be obtained.

Outside the framework of X-ray imaging, we recommend that the method described in this paper is also an effective diagnostic tool in simulation of KHW. $dI(\phi, \theta)$ defined in equation (3) enables the quantitative analysis of numerical data and thus helps to reveal the global features of KHW. Moreover, Figure 3 and equation (2) imply that the parameter $dI(\phi, \theta)$ has direct physical meanings: it represents the efficiency of KHW induced plasma mixture or transportation in the magnetopause boundary layer.

4.2. Background Processing

The method in this paper deals with pure geocoronal SWCX emissions from simulation, whereas in realistic observations they are superposed on other X-ray signals, such as the cosmic and heliospheric sources. Therefore, knowledge of the background emissions is needed before extracting KHW information.

As introduced in section 1, three features of the geocoronal SWCX emission help to distinguish it from other diffuse X-ray sources. Consequently, the period with apparently high geocoronal SWCX emission can be selected out in the first place. Then the difference spectrum is produced by subtracting the background observed during the SWCX-insignificant period from the former signal, which approximates the lower limit of the SWCX enhancement [*Carter et al.*, 2011]. Afterward, based on this difference spectrum, KHW signals may be extracted by using the method described in this paper.

The above process is based on the fact that diffuse X-ray sources outside the heliosphere (galactic and extragalactic sources) are generally expected to be independent of time [*Cravens*, 2000]. Moreover, the heliospheric emissions caused by SWCX with heliospheric neutral atoms also have weaker time variability than geocoronal SWCX [*Cravens et al.*, 2001]. Specifically, the time scale of the X-ray variations emitted from heliospheric helium is about a day or two and the heliospheric hydrogen sources vary over a couple of weeks according to *Cravens et al.* [2001]. Therefore, they can be viewed as steady background when analyzing geocoronal SWCX X-rays varying on minutes and thus could be filtered out when analyzing real satellite data [*Robertson and Cravens*, 2003b].

4.3. Requirements for KHW Imaging and Instrument Simulation

Based on the present case, it is noted that the detection of KHW using the X-ray imaging technique has the following requirements. First, the X-ray telescope should have a wide FOV. Figure 4c indicates a latitudinal FOV (θ direction) no smaller than 20° and a longitudinal FOV (ϕ direction) no smaller than 25° to reveal the global configuration of KHW. Second, in order to resolve the transient phenomenon the interval to record the X-ray intensity should be on the time scale of minutes. Third, the detector should be able to resolve the maximum X-ray intensity induced by KHW, i.e., $dI_{meq} \sim 2.0$ keV cm^{-2} s^{-1} sr^{-1} in Figure 3.

©2014. American Geophysical Union. All Rights Reserved.

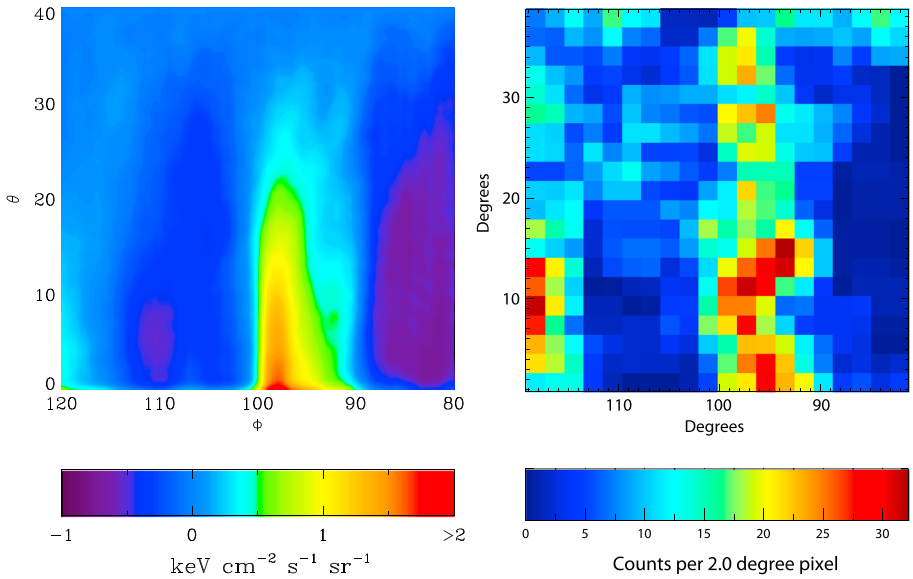

Figure 6. (left) X-ray intensity (d*I*) at t = 893 s and (right) the simulated X-ray counts converted by using an X-ray telescope simulator.

X-ray telescope making use of the Lobster eye optic makes these requirements possible. It is sensitive to the 0.2 to 4 keV energy range, covering the soft X-ray band of SWCX emission. The Lobster eye optics employ an ingenious system of reflective optics based on square microchannels arrayed in a curved surface, which have a theoretical FOV up to 4π sr. They allow the signal/noise ratio to be increased compared to nonfocusing devices [*Peele et al.*, 2004; *Gorenstein*, 1987].

To better prove that the KHW induced X-ray enhancement is detectable, the modeled SWCX emission was converted into observed X-ray counts by using an X-ray telescope simulator. We have assumed a configuration which is achievable with existing technology and which is similar to the imager on the proposed AXIOM (Advanced X-ray Imaging of the Magnetosphere) concept [*Branduardi-Raymont et al.*, 2012]. The simulator assumes an optic which uses square-channel micropore plates in a Lobster eye configuration [*Brunton et al.*, 1997]. The assumed focal length of the optic is 1.0 m. The detector is assumed to have the quantum efficiency characteristics of a back-illuminated charge-coupled device (CCD) and has an optical/UV filter as required by astrophysical X-ray telescopes. The combined QE/filter combination is essentially identical to the EPIC-PN instrument with the medium filter on XMM-Newton [*Struder et al.*, 2001]. The total effective area of the instrument at 500 eV is 94 cm^2.

The simulator adds a flat background component characteristic of the soft X-ray astrophysical background. This is spatially variable on large scales but has been well mapped by ROSAT. We have assumed a spectral model derived from XMM-Newton data with an intensity typical of a viewing direction on the ecliptic plane. Folding our background spectrum through the ROSAT-position sensitive proportional counter response gives a count rate of 500×10^{-6} cts s^{-1} arc min^{-2} which is typical of the observed rates seen by ROSAT for viewing directions along the ecliptic. In addition, a particle-induced background component in the detector of 0.02 cts cm^{-2} s^{-1} is assumed, characteristic of a CCD-based instrument in LEO (Swift XRT instrument team, private communication, 2014). Figure 6 shows the simulation results for an assumed exposure of 180 s and has the appropriate level of Poisson noise. A "local" background model, which is a smooth function of counts per pixel versus ϕ, is derived from the data at $\theta \sim 40°$. This model is then subtracted from the entire image to reveal the KHW enhancement. Figure 6 is dI at $t = 893$ s (left) and the simulated X-ray counts (right). It is shown that KHW-induced X-ray is evident at $\phi \sim 98°$, which provides vital support for the conclusion that X-ray imaging is a promising technique to detect KHW.

4.4. Significance of X-ray Imaging of the Magnetospheric System

Unlike the traditional in situ observation detecting local plasma conditions, application of the X-ray imaging technique in magnetospheric physics will directly reveal the configurations and evolutions in a global scale. Moreover, studies of geocoronal SWCX X-ray emission can help to provide local information

©2014. American Geophysical Union. All Rights Reserved.

on the solar wind in addition to the monitors such as ACE [*Carter et al.*, 2010]. Recognizing its promising prospects, several concept missions focusing on X-ray imaging of the magnetosphere have been proposed (e.g., STORM [*Collier et al.*, 2012], AXIOM [*Branduardi-Raymont et al.*, 2012], and AXIOM-Jian proposal submitted to the Chinese Academy of Sciences-European Space Agency Joint Scientific Space Mission recently).

Besides magnetospheric investigations, the X-ray imaging technique is also of astrophysical interest. Quantitative studies on the geocoronal SWCX emissions, considered as contamination for cosmological analysis, can help to eliminate these background signals from astronomical observations.

5. Conclusion

X-ray emissions can be produced in the magnetosheath by the SWCX process between heavy solar wind ions and geocoronal hydrogen. At the flank magnetopause where KH vortices develop, high-density spikes intruding from the magnetosheath toward the magnetosphere lead to local maxima of the X-ray intensity according to global MHD simulation. This paper proposed a method to extract this KHW-related information from the simulated X-ray intensity detected by a hypothetical X-ray telescope onboard a LEO satellite, i.e., the X-ray intensity at high latitude is subtracted as a background to highlight the signal from KHW. By analyzing the simulated X-ray intensity, we quantitatively present the velocity, perturbation level, longitudinal, and latitudinal distributions of a typical KH vortex and their temporal evolutions, which is significant for the understanding of momentum transportation or plasma mixing across the low-latitude boundary layer. Moreover, the efficiency of this method during intervals of solar wind disturbances is verified. The numerical results thus suggest that the X-ray imaging technique is a promising way to directly observe the large-scale configuration and evolution of KHW. Also discussed in the paper is a preliminary analysis on background processing and requirements to resolve KHW in the soft X-ray spectrum.

Acknowledgments

We would like to thank Y.Q. Hu for providing information on the MHD simulation code, from which the data used in this study are derived. All the analyzed data can be accessed by contacting the authors (email: trsun@spaceweather.ac.cn; cw@spaceweather.ac.cn). The authors also acknowledge W. Yuan and Z. Ling from National Astronomical Observatories (Chinese Academy of Sciences), as well as G. Branduardi-Raymont from University College London for their information on the diffuse X-ray background. This work was supported by 973 program 2012CB825602, NNSFC grant 41304131, and in part by the Specialized Research Fund for State Key Laboratories of China.

Yuming Wang thanks the reviewers for their assistance in evaluating this paper.

References

Bhardwaj, A., et al. (2007), X-rays from solar system objects, *Planet. Space Sci.*, *55*, 1135–1189.

Branduardi-Raymont, G., et al. (2012), AXIOM: Advanced X-ray imaging of the magnetosphere, *Exp. Astron.*, *33*, 403–443, doi:10.1007/s10686-011-9239-0.

Brunton, A. N., G. W. Fraser, J. E. Lees, and I. C. E. Turcu (1997), Metrology and modeling of microchannel plate X-ray optics, *Appl. Opt.*, *36*, 5461–5470.

Carter, J., and S. Sembay (2008), Identifying XMM-Newton observations affected by solar wind charge exchange—Part I, *Astron. Astrophys.*, *489*, 837–848.

Carter, J., S. Sembay, and A. M. Read (2010), A high charge state coronal mass ejection seen through solar wind charge exchange emission as detected by XMM-Newton, *MNRAS*, *402*, 867–878.

Carter, J., S. Sembay, and A. M. Read (2011), Identifying XMM-Newton observations affected by solar wind charge exchange—Part II, *Astron. Astrophys.*, *527*, A115.

Collier, M. R., D. G. Sibeck, T. E. Cravens, I. P. Robertson, and N. Omidi (2010), Astrophysics noise: A space weather signal, *Eos Trans. AGU*, *91*(24), 709–722.

Collier, M. R., et al. (2012), Prototyping a global soft X-ray imaging instrument for heliophysics, planetary science, and astrophysics science, *Astron. Nachr.*, *4*, 378–382, doi:10.1002/asna.201211662.

Collier, M. R., et al. (2014), On lunar exospheric column densities and solar wind access beyond the terminator from ROSAT soft X-ray observations of solar wind charge exchange, *J. Geophys. Res. Planets*, *119*, 1459–1478, doi:10.1002/2014JE004628.

Contin, J. E., F. T. Gratton, and C. J. Farrugia (2003), Theoretical results on the latitude dependence of the Kelvin-Helmholtz instability at the dayside magnetopause for northward interplanetary magnetic fields, *J. Geophys. Res.*, *108*(A6), 1227, doi:10.1029/2002JA009319.

Cowee, M. M., D. Winske, and S. P. Gary (2010), Hybrid simulations of plasma transport by Kelvin-Helmholtz instability at the magnetopause: Density variations and magnetic shear, *J. Geophys. Res.*, *115*, A06214, doi:10.1029/2009JA015011.

Cox, D. P. (1998), Modeling the local bubble, in *The Local Bubble and Beyond*, edited by D. Breitschwerdt, M. J. Freyberg, and J. Trümper, p. 121, Springer, New York.

Cravens, T. E. (1997), Comet Hyakutake X-ray source: Charge transfer of solar wind heavy ions, *Geophys. Res. Lett.*, *24*(1), 105–108.

Cravens, T. E. (2000), Heliospheric X-ray emission associated with charge transfer of the solar wind with interstellar neutrals, *Astrophys. J.*, *532*, L153–L156.

Cravens, T. E., I. P. Robertson, and S. L. Snowden (2001), Temporal variations of geocoronal and heliospheric X-ray emission associated with the solar wind interaction with neutrals, *J. Geophys. Res.*, *106*, 24,883–24,892.

Dennerl, K., C. M. Lisse, A. Bhardwaj, V. Burwitz, J. Englhauser, H. Gunell, M. Holmström, F. Jansen, V. Kharchenko, and P. M. Rodríguez-Pascual (2006), First observation of Mars with XMM-Newton: High resolution X-ray spectroscopy with RGS, *Astron. Astrophys.*, *451*, 709–722.

Ezoe, Y., Y. Miyoshi, H. Yoshitake, K. Mitsuda, N. Terada, S. Oishi, and T. Ohashi (2011), Enhancement of terrestrial diffuse X-ray emission associated with coronal mass ejection and geomagnetic storm, *Publ. Astron. Soc. Jpn.*, *63*, 691–704.

Fujimoto, R., et al. (2007), Evidence for solar-wind charge-exchange X-ray emission from the Earth's magnetosheath, *Publ. Astron. Soc. Japan*, *59*, 133–140.

Gorenstein, P. (1987), All sky supernova and transient explorer (ASTRE), in *Variability of Galactic and Extragalactic X-ray Sources*, edited by A. Treves, p. 253, Associazione per LAvanzamento dell Astronomia, Milano-Bologna, Italy.

©2014. American Geophysical Union. All Rights Reserved.

Guo, X. C., C. Wang, and Y. Q. Hu (2010), Global MHD simulation of the Kelvin-Helmholtz instability at the magnetopause for northward interplanetary magnetic field, *J. Geophys. Res.*, *115*, A10218, doi:10.1029/2009JA015193.

Hasegawa, H., M. Fujimoto, T. D. Phan, H. Reme, A. Balogh, M. W. Dunlop, C. Hashimoto, and R. TanDokoro (2004), Transport of solar wind into Earth's magnetosphere through rolled-up Kelvin-Helmholtz vortices, *Nature*, *430*(7001), 755–758, doi:10.1038/nature02799.

Hu, Y. Q., X. C. Guo, and C. Wang (2007), On the ionospheric and reconnection potentials of the Earth: Results from global MHD simulations, *J. Geophys. Res.*, *112*, A07215, doi:10.1029/2006JA012145.

Hwang, K.-J., M. L. Goldstein, M. M. Kuznetsova, Y. Wang, A. F. Viñas, and D. G. Sibeck (2012), The first in situ observation of Kelvin-Helmholtz waves at high-latitude magnetopause during strongly dawnward interplanetary magnetic field conditions, *J. Geophys. Res.*, *117*, A08233, doi:10.1029/2011JA017256.

Li, W., J. Raeder, M. F. Thomsen, and B. Lavraud (2008), Solar wind plasma entry into the magnetosphere under northward IMF conditions, *J. Geophys. Res.*, *113*, A04204, doi:10.1029/2007JA012604.

Li, W., C. Wang, B. Tang, X. Guo, and D. Lin (2013), Global features of Kelvin-Helmholtz waves at the magnetopause for northward interplanetary magnetic field, *J. Geophys. Res. Space Physics*, *118*, 5118–5126, doi:10.1002/jgra.50498.

Lisse, C. M., et al. (1996), Discovery of X-ray and extreme ultraviolet emission from Comet C/Hyakutake, *Science*, *274*, 205–209.

Nishino, M. N., et al. (2011), A case study of Kelvin-Helmholtz vortices on both flanks of the Earth's magnetotail, *Planet. Space Sci.*, *59*(7), 502–509.

Peele, A. G., H. Lyngsjo, R. M. Crocker, J. Markham, N. Bannister, and K. A. Nugent (2004), Modeling of the Lobster-ISS X-ray telescope in orbit, paper SPIE 5488 presented at UV and Gamma-Ray Space Telescope Systems.

Pepino, R., V. Kharchenko, A. Dalgarno, and R. Lallement (2004), Spectra of the X-ray emission induced in the interaction between the solar wind and heliospheric gas, *Astrophys. J.*, *617*, 1347–1352.

Robertson, I. P., and T. E. Cravens (2003a), Spatial maps of heliospheric and geocoronal X-ray intensities due to the charge exchange of the solar wind with neutrals, *J. Geophys. Res.*, *108*(A10), 8031, doi:10.1029/2003JA009873.

Robertson, I. P., and T. E. Cravens (2003b), X-ray emission from the terrestrial magnetosheath, *Geophys. Res. Lett.*, *30*(8), 1439, doi:10.1029/2002GL016740.

Robertson, I. P., M. R. Collier, T. E. Cravens, and M.-C. Fok (2006), X-ray emission from the terrestrial magnetosheath including the cusps, *J. Geophys. Res.*, *111*, A12105, doi:10.1029/2006JA011672.

Snowden, S. L., M. R. Collier, T. Cravens, K. D. Kuntz, S. T. Lepri, I. Robertson, and L. Tomas (2009), Observation of solar wind charge exchange emission from exospheric material in and outside Earth's magnetosheath 2008 September 25, *Astrophys. J.*, *691*, 372–381.

Struder, L., et al. (2001), The European photon imaging camera on XMM-Newton: The pn-CCD camera, *A&A*, *365*, L18–L26.

Taylor, M. G. G. T., et al. (2012), Spatial distribution of rolled up Kelvin-Helmholtz vortices at Earth's dayside and flank magnetopause, *Ann. Geophys.*, *30*, 1025–1035, doi:10.5194/angeo-30-1025-2012.

Wargelin, B. J., M. Markevitch, M. Juda, V. Kharchenko, R. Edgar, and A. Dalgarno (2004), Chandra observations of the dark moon and geocoronal solar wind charge transfer, *Astrophys. J.*, *607*, 596–610.

©2014. American Geophysical Union. All Rights Reserved.